

On the Aging Behavior of Ti-1.0 wt pct Fe Alloy With an Equiaxed $\alpha + \beta$ Initial Microstructure



YAN CHONG, JANGHO YI, GUANYU DENG, and NOBUHIRO TSUJI

The aging behavior (300 °C to 700 °C) of Ti-1.0 wt pct Fe alloy was investigated in this study, by means of various microstructural characterization techniques and micromechanical testing methods. The initial microstructure consisted of equiaxed α and β grains as well as athermal ω precipitates (ω_{ath}) with several tens of nanometers inside β grains. During the aging process, significant microstructural modifications took place within the β grains. At relatively lower aging temperatures (300 °C to 500 °C), the volume fraction of ω_{ath} gradually decreased with increasing aging temperature, until they were totally replaced by secondary α precipitates (α_s) at 500 °C. With further increase of the aging temperature (500 °C ~ 700 °C), the size of α_s precipitates substantially increased while the volume fraction gradually decreased, indicating a partial α to β reverse phase transformation. At aging temperatures higher than 600 °C, the re-precipitation of ω_{ath} from reverse-transformed β phase during water quench was identified. Due to an extremely high Fe concentration of these ω_{ath} that inherited from reverse-transformed β phase, their lattice constants were much smaller than those in the initial microstructure. The existence of ω_{ath} inside β phase promoted a homogeneous precipitation behavior of α_s precipitates during aging, by providing much more potential intragranular nucleation sites. This led to the formation of plate-shaped α_s precipitates with multiple crystallographic variants, in sharp contrast to the conventional α lamellar/colony structure with limited crystallographic variants obtained by thermomechanical processing in which α_s precipitates directly transformed from β phase. Moreover, it was also revealed that the transformation of nano-sized ω_{ath} into α_s precipitates as well as their subsequent coarsening led to a continuous decrease of the nano-hardness of prior β areas.

<https://doi.org/10.1007/s11661-023-07030-y>

© The Minerals, Metals & Materials Society and ASM International 2023

I. INTRODUCTION

TITANIUM alloys possessed a number of highly desirable properties, *e.g.*, high specific strength and good corrosion resistance, making them attractive structural materials in the weight and corrosion-sensitive applications.^[1–4] Among the various titanium alloys, Ti-Fe

binary alloys have recently drawn particular attention with respect to the microstructure evolution during thermomechanical processing^[5,6] and the phase transformation behaviors during high-pressure torsion (HPT)^[7–11] as well as annealing.^[12–14] Iron, as a strong β -stabilizing element, is commonly found as an impurity in commercially pure titanium. Even with a relatively small amount, the iron addition can significantly lower the β -transus temperature, thus, introducing introduce an $\alpha + \beta$ two-phase region in the Ti-Fe binary phase diagram.^[15–22] By applying thermomechanical processing in the two-phase region, α -lamellae in the as-cast microstructure of Ti-Fe alloys can be transformed into equiaxed $\alpha + \beta$ dual-phase microstructures, exhibiting a good balance between strength and ductility.^[5,23] The application of thermomechanical processing also allows for the fabrication of ultrafine-grained (UFG) equiaxed $\alpha + \beta$ dual-phase microstructures in dilute Ti-Fe binary alloys, exhibiting comparable mechanical properties to some of the $\alpha + \beta$ titanium alloys,^[23] while the alloying element is much cheaper in the former. It has been revealed that the high strength of UFG equiaxed $\alpha + \beta$ dual-phase microstructures in Ti-Fe alloys originated

YAN CHONG and NOBUHIRO TSUJI are with the Department of Materials Science and Engineering, Kyoto University, Kyoto 606-8501, Japan and also with the Elements Strategy Initiative for Structural Materials (ESISM), Kyoto University, Kyoto 606-8501, Japan. Contact e-mail: chong.yan.6w@kyoto-u.ac.jp JANGHO YI is with the Department of Materials Science and Engineering, Kyoto University and also with the National Institute of Materials Science, Tsukuba, Ibaraki 305-0047, Japan. GUANYU DENG is with the Department of Materials Science and Engineering, Kyoto University and also with the School of Mechanical, Materials, Mechatronic and Biomedical Engineering, University of Wollongong, Wollongong, NSW 2522, Australia

Manuscript submitted December 16, 2022; accepted February 24, 2023.

Article published online March 19, 2023

from both the ultrafine grain size and a large number density of athermal ω precipitates (ω_{ath}) with several tens of nanometers inside β grains.^[5,23] The formation of ω_{ath} inside β grains has been attributed to the high Fe concentration inside. As a matter of fact, both the high Fe concentration and nano-sized ω_{ath} contributed to a much larger nano-hardness of β grains than α grains in the dual-phase Ti-Fe microstructure.^[5] Moreover, the two phases also showed dramatically different phase transformation behaviors during HPT deformation and subsequent annealing process, such as the kinetics of shear-induced α or β to ω phase transformation, and their related thermal stability upon annealing.^[7–14]

In addition to the significant hardening effect to β phase, the existence of fine ω_{ath} was also supposed to alter the aging response of β phase, which in turn affected the micromechanical behaviors of $\alpha + \beta$ dual-phase microstructures of Ti-Fe alloy. In the previous studies of metastable β titanium alloys,^[24–30] it has been reported that ω_{ath} in the as-quenched β grains would substantially influence the morphology, transformation pathway, as well as crystallographic orientations of α precipitates during the aging process. A slower heating rate and two-step aging process have proved to be effective in refining the size of intragranular α precipitates. The mechanisms for super-refined intragranular α precipitates were also comprehensively discussed through detailed characterizations of high-resolution transmission electron microscopy and atom probe tomography.^[25–27] Despite of the fact that the bulk chemical composition of dilute Ti-Fe binary alloys is much closer to pure Ti, the β grains in the dual-phase microstructure were indeed extremely rich in β -stabilizing element (Fe) and ω_{ath} as well, both of which make them comparable to the as-quenched single-phase metastable β titanium alloys, especially when considering the aging response. Nonetheless, there have been no relevant studies on the microstructure evolution and phase transformation behaviors during the aging process of Ti-Fe alloys with an equiaxed $\alpha + \beta$ dual-phase initial microstructure, which brings forth the key motivation of this study.

To this end, in this study, a thorough investigation on the aging behaviors (300 °C ~ 700 °C), including microstructural evolution, phase transformation, and micromechanical property change of Ti-1.0 wt pct Fe alloy with an equiaxed $\alpha + \beta$ initial microstructure was carried out for the first time. By specifically designed thermomechanical-processing routes, the influence of ω_{ath} on precipitation behaviors of secondary α phase was examined in detail, from the perspectives of both microstructure characteristics and crystallographic variant selections. The redistribution of Fe solutes between different phases during aging as well as its influence on the lattice constants was also briefly discussed.

II. MATERIALS AND EXPERIMENTAL METHODS

Ti-1.0Fe ingot with a bulk composition of Ti-1.0 wt pct Fe-0.06 wt pct O ($T_{\beta} \sim 870$ °C) was used in this

study. Cylinder samples ($\Phi 8 \times 12$ mm) machined from the ingot were β annealed at 940 °C for 1 hour followed by water quench. The cylinder samples were then uniaxially compressed at 800 °C with a strain rate of 10^{-4} s^{-1} until a true strain of -0.8 , followed by immediate water quench. Equiaxed $\alpha + \beta$ dual-phase microstructure (Figure 1) was obtained after the hot deformation, which was used as the initial microstructure for subsequent aging treatments. Details of the initial microstructure can be found in detail in our previous study.^[5]

Aging treatments were conducted at 300 °C, 400 °C, 500 °C, 600 °C, 650 °C and 700 °C for 1 hour in vacuum followed by water quench. For microstructural characterization, slices cut from the center of the aged specimens were prepared by mechanical polishing and then electro-polishing in a perchloric acid methanol solution (volume ratio of 1:9) at -30 °C. Microstructural observations, including scanning electron microscopy (SEM) and electron backscattered diffraction (EBSD), were carried out on a field-emission gun SEM (JEOL 7100F) equipped with TSL system. Energy-dispersive X-ray spectroscopy (EDX) mappings of Fe and Ti atoms were conducted using EDAX system attached to the JEOL 7100F SEM. More than 30 grains were examined for both phases to obtain the average chemical compositions. X-ray diffraction (XRD) analysis was done on a PANalytical X'Pert-ProMPD system with Cu- K_{α} radiation. Transmission electron microscopy (TEM) samples were first mechanical-polished to a thickness of ~ 100 μm , followed by a standard twin-jet electro-polishing at -40 °C with a voltage of 20 V, in a solution of 5 pct perchloric acid, 35 pct n-Butanol, and 60 pct methanol. TEM characterizations were conducted on a JEOL 3010 TEM operated at 300 kV.

The nano-hardness measurements of α grains and prior β areas in the aged microstructures were conducted using a Hysitron TI950 Triboindenter system equipped with a three-sided Berkovich diamond indenter tip. 400 indentations (in the form of 20×20 matrix) covering an area of 60×60 μm^2 were performed on the electro-polished surfaces. Four locations over a distance of 500 μm were examined for each microstructure, and the averaged nano-hardness values were calculated for each phase (area). Each indentation was carried out by a load-control mode, with a peak load of 1000 μN and holding time of 10 seconds. Locations of the indents (either inside the α grains or prior β areas) were carefully checked in the SEM image taken after indentation. Indents lying near the prior α/β interphase boundaries were excluded from the calculation.

III. RESULTS AND DISCUSSION

A. Microstructure Evolution and Phase Transformation During Aging

The equiaxed $\alpha + \beta$ initial microstructure before aging is shown in Figure 1. It consisted of equiaxed α grains [vol. pct (α) = 82 pct, $D(\alpha) = 12.2$ μm] and β grains [vol. pct (β) = 18 pct, $D(\beta) = 4.7$ μm], which

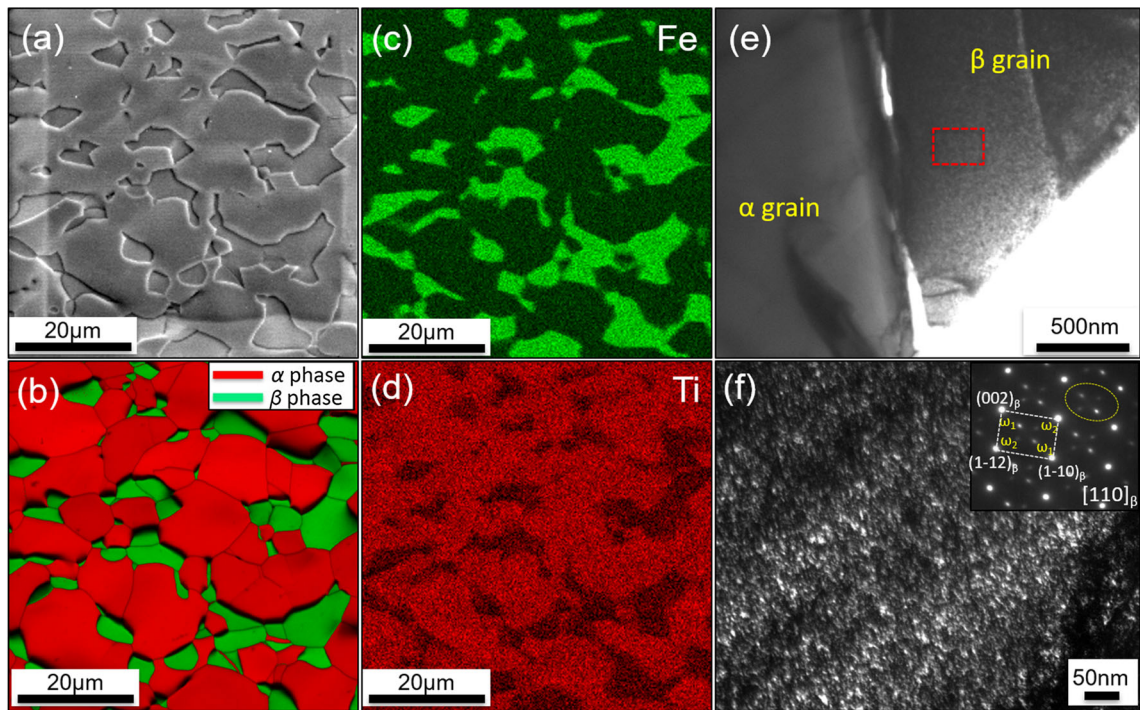


Fig. 1—Initial microstructure of Ti-1.0Fe alloy before aging. (a) BSE image, in which the convex and concave areas were α and β phases, respectively. (b) The corresponding phase map (α : red, β : green) of the same area are shown. EDX mappings of Fe (c) and Ti (d) for the same area are shown. (e) TEM image showing α and β grains. Nano-sized precipitates with a high density were observed inside the β grain, adapted from Ref. [5]. (f) Dark-field image using the extra spots of ω phase, as circled in the diffraction pattern inserted, taken from $[110]_{\beta}$ zone axis. A large number of athermal ω precipitates with a size of several tens of nanometers were highlighted inside the β grain, adapted from Ref. [5] (Color figure online).

were shown as convex and concave areas in the backscattered electron (BSE) image [Figure 1(a)], respectively. The corresponding phase map (α phase: red, β phase: green) of the same area is shown in Figure 1(b). The related EDX mappings of Fe and Ti atoms of the same area are shown in Figures 1(c) and (d), respectively, in which a strong Fe partitioning in β phase was observed. The average Fe concentrations of α and β phases were measured to be 0.24 wt pct and 4.6 wt pct, respectively. Accordingly, the average Ti concentration in β phase was slightly lower than that in α phase. In the TEM image [Figure 1(e)], the α grain was quite clean, whereas a large density of fine precipitates was clearly observed inside the β grain. In the diffraction pattern of β grain taken from a zone axis of $[110]_{\beta}$ [as inserted in Figure 1(f)], extra spots corresponding to athermal ω phase was clearly identified at the locations of $1/3 < 21-1 >$ and $2/3 < 21-1 >$ of β matrix.^[24–30] The corresponding dark-field (DF) image using the extra spots of athermal ω phase clearly highlighted the existence of nano-sized (~ 20 nm) athermal ω precipitates (ω_{ath}) with a homogenous distribution [Figure 1(f)]. According to the previous studies of metastable β titanium alloys,^[29,30] the ω_{ath} formed during water quench generally maintained the same chemical composition as the parent β phase. It is, thus, reasonable to assume that the high Fe concentration of β grains in the initial dual-phase microstructure was also inherited by the ω_{ath} that formed inside. Therefore, the

initial microstructure of Ti-1.0Fe alloy before aging was a mixture of equiaxed α and β grains, as well as ω_{ath} with a size of several tens of nanometers inside the β grains.

BSE images of samples aged at 300 °C~ 700 °C are shown in Figure 2. Images with a larger magnification were inserted to show the microstructural details inside the β grains. In general, there was no evident microstructural modification inside the α grains (convex areas) for all the aging temperatures. Inside the β grains (concave areas), on the other hand, extremely fine precipitates began to appear from the aging temperature of 500 °C [Figure 2(c)]. At higher aging temperatures (600 °C ~ 700 °C) [Figure 2(d) ~ (f)], plate-shaped precipitates can be clearly observed inside the β grains. With increasing aging temperature, the size of plate-shaped precipitates gradually increased, while the number density and area fraction continuously decreased. Despite of that, the area/size of prior β grains (including the secondary precipitates and retained β , referred to as prior β area hereafter) in the aged microstructures did not change with aging temperature.

The phase transformation behavior was also systematically investigated by XRD analysis, as shown by the diffraction patterns [Figure 3(a)]. Fine scans of these microstructures within 2θ angles of $37^{\circ} \sim 42^{\circ}$ are shown in Figure 3(b). Before aging, diffraction peaks corresponded to α (10-10), α (10-11), α (10-2), β (110), and ω (11 - 20 + 10 - 11) were clearly identified, confirming the co-existence of α , β , and ω phases in the initial

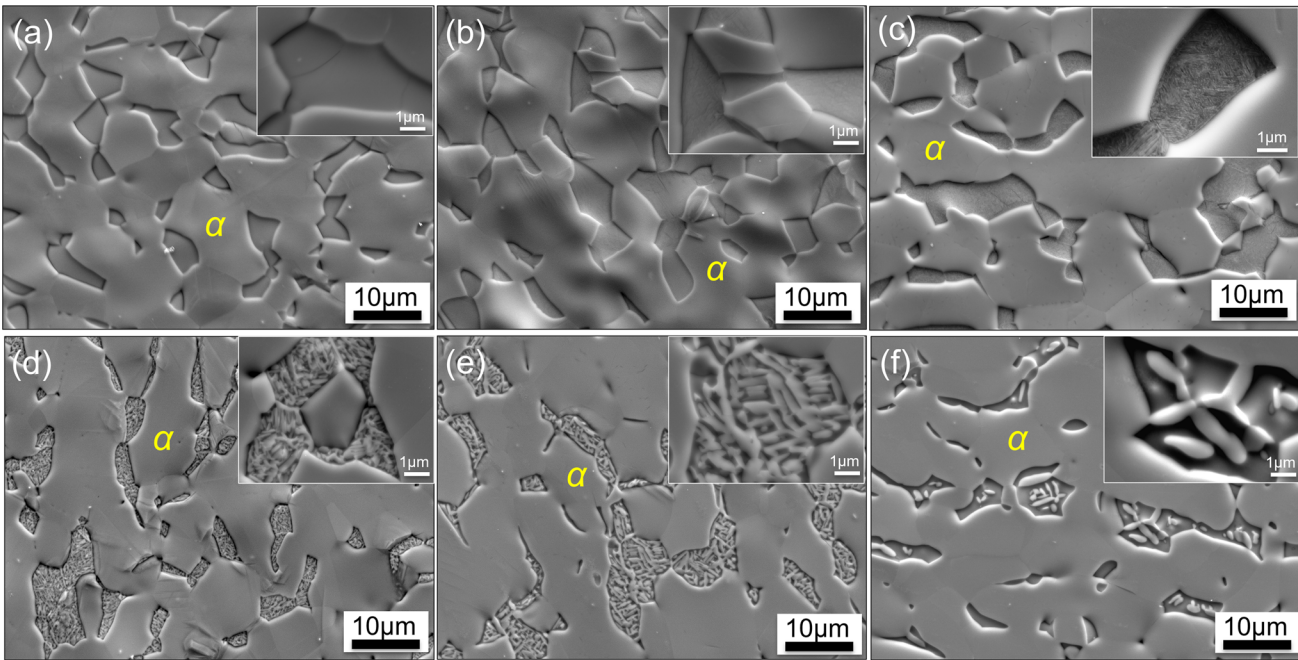


Fig. 2—BSE images of samples aged at 300 °C (a), 400 °C (b), 500 °C (c), 600 °C (d), 650 °C (e), and 700 °C (f) for 1 hour followed by water quench. Images with a larger magnification are also inserted. The convex and concave areas in the images corresponded to α grains and prior β areas, respectively. Fine precipitates began to appear inside β grains from the aging temperature of 500 °C.

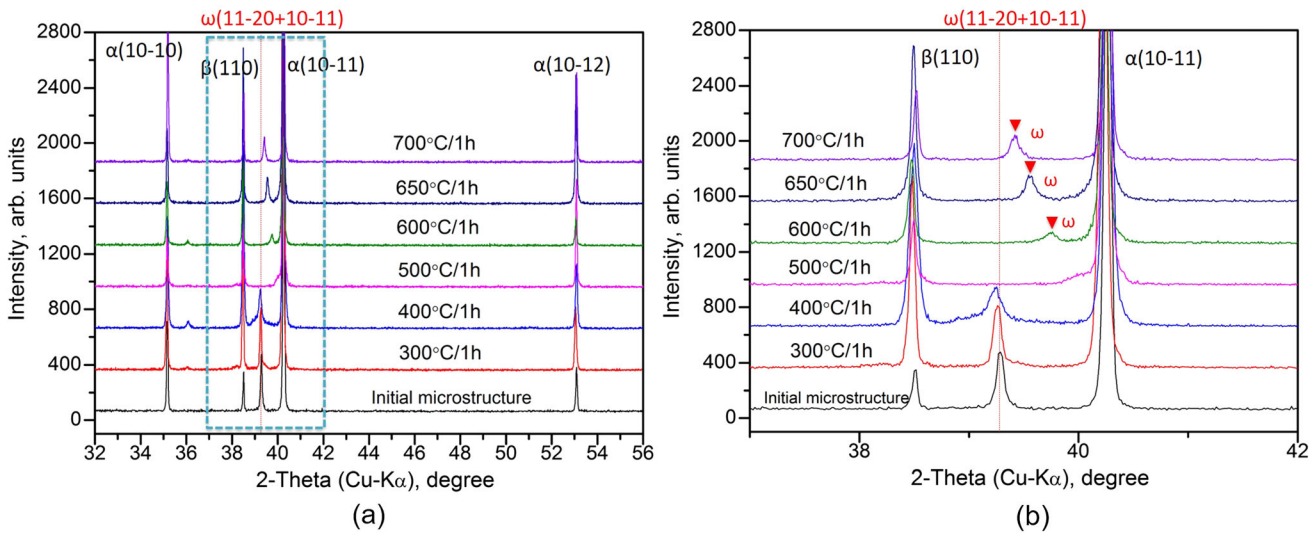


Fig. 3—(a) XRD patterns of the samples before and after aging. (b) Fine scans (2θ : 37° ~ 42°) showing the detailed locations and peak shift of ω phase. The peak intensity of ω phase in the initial microstructure gradually decreased with increasing aging temperature until it totally disappeared at 500 °C. From the aging temperature of 600 °C, ω phase peak appeared again at a 2θ angle much larger than its original position in the initial microstructure. With increasing aging temperature, the peak intensity of this newly formed ω phase gradually increased with peak position shifting towards a smaller 2θ angle.

microstructure. Upon aging, the peak intensity of ω phase continuously decreased until it totally disappeared at the aging temperature of 500 °C, which indicated a solvus temperature of athermal ω phase between 400 °C and 500 °C in Ti-1.0Fe alloy. In addition, the peak position of ω phase also slightly shifted towards a smaller 2θ angle with increasing aging temperature below 500 °C. At the aging temperature of 600 °C, ω phase peak with a much lower peak intensity appeared

again at a 2θ angle $\sim 0.5^\circ$ larger than its original position in the initial microstructure. With further increase of the aging temperature, the peak position of newly formed ω phase gradually shifted towards a smaller 2θ angle, although it still located to the right of its original position in the initial microstructure. At the same time, its peak intensity slightly increased with increasing aging temperature. These variations in ω phase peak clearly suggested that the properties of newly

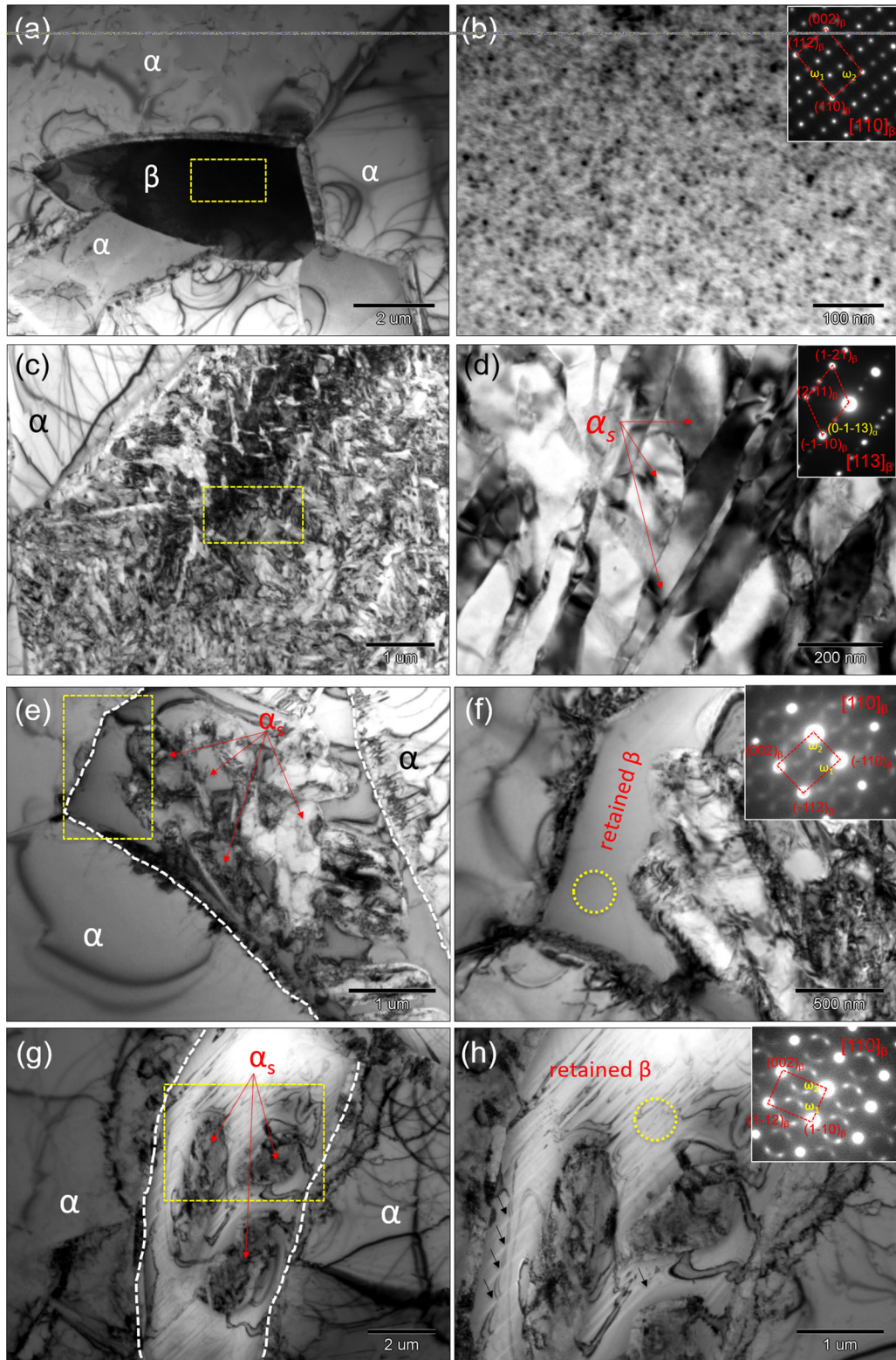


Fig. 4—TEM bright-field images of the microstructures aged at 300 °C (*a* and *b*), 500 °C (*c* and *d*), 650 °C (*e* and *f*), and 700 °C (*g* and *h*). Spherical ω precipitates were replaced by plate-shaped secondary α precipitates from the aging temperature of 500 °C. Athermal ω phase re-precipitated inside the retained β at higher aging temperatures. Band-like contrasts [indicated by black arrows in (*h*)] were frequently observed inside the retained β phase at the aging temperature of 700 °C. The prior β areas boundaries in the 650 °C (*e*) and 700 °C (*g*) aged microstructures were indicated by white-dashed lines (Color figure online).

formed ω phase were quite sensitive to the aging temperature, for which both the volume fraction and lattice constants gradually increased with increasing aging temperature.

To further explore the microstructure evolution and phase transformation occurred during aging, some of the aged microstructures were also characterized by TEM (Figure 4). In the specimen aged at 300 °C [Figures 4(a) and (b)], ω precipitates with a large number density were still present inside the β grain, with a marginally larger precipitate size than those in the initial microstructure. In the previous literature of metastable β titanium alloys,^[29,30] it has been confirmed that by aging the as-quenched microstructures at relatively lower temperatures (below ω -solvus temperature), the supersaturated β -stabilizing elements (*i.e.*, Fe and V *et al.*) inside the athermal ω precipitates would gradually diffuse into the β matrix, leading to the formation of so-called thermal ω precipitates with a chemical composition close to the equilibrium state. Furthermore, due to a smaller atomic radius of substitutional Fe atoms (0.126 nm) than Ti atoms (0.147 nm), the rejection of Fe atoms from athermal ω precipitates would cause a slight lattice expansion in the resulting thermal ω phase. This was reflected in the slight peak shift of ω phase (towards a smaller 2θ angle) in the 300 °C and 400 °C aged microstructures compared with that in the initial microstructure [Figure 3(b)]. In the specimen aged at 500 °C [Figures 4(c) and (d)], the nano-sized spherical ω precipitates were replaced by plate-shaped precipitates with a much larger size (average thickness \sim 100 nm). These plate-shaped precipitates were confirmed to be α phase (referred to as secondary α precipitates hereafter) by the diffraction pattern [Figure 4(d)]. The extra spots corresponding to ω phase were absent at this aging temperature. This is in a good agreement with the XRD results, in which the diffraction peaks of ω phase disappeared at the aging temperature of 500 °C. It is also worth noting that these secondary α precipitates inside β grain showed a rather weak variant selection [Figures 4(c) and 2(d)], in sharp contrast to the typical α lamellar/colony microstructure found in $\alpha + \beta$ titanium alloys.^[27–30] This implies that the pre-existing athermal ω precipitates inside the β grain could possibly affect the nucleation and growth behaviors of secondary α precipitates, which will be explored in detail in the discussion part of this study.

In the specimen aged at 650 °C [Figures 4(e) and (f)], the size of secondary α precipitates substantially increased while their number density and area fraction decreased compared with those in the 500 °C aged specimen. The reduced area fraction of secondary α precipitates was due to a partial α to β reverse phase transformation at higher aging temperatures. The reverse-transformed β phase was mostly retained after water quench, mainly locating around the original α/β interphase boundaries. In the diffraction pattern of retained β phase [as circled in Figure 4(f)], extra spots corresponding to athermal ω phase were identified (as circled by red dotted lines), indicating a re-precipitation of athermal ω from the reverse-transformed β phase during the water quench process after aging. This was

consistent with the XRD results, in which the disappeared ω phase peak (at 500 °C) was detected again from the aging temperature of 600 °C (Figure 3). However, these athermal ω precipitates were hardly visible in the TEM images [Figures 4(e) and (f)], probably due to their extremely fine size and low density. At the aging temperature of 700 °C [Figures 4(g) and (h)], the number density and area fraction of secondary α precipitates further decreased, with only a few of them remaining inside the prior β grain. In the diffraction pattern [Figure 4(h)] of retained β phase [as circled in Figure 4(h)], the extra spots corresponding to athermal ω precipitates were identified again (as circled by red dotted lines), and the intensity of extra spots was relatively higher than that in the 650 °C aged microstructure. This probably indicated a relatively higher volume fraction of ω phase forming from the retained β phase in the 700 °C aged microstructure, also being consistent with the XRD results (Figure 3).

B. Fe Redistribution and Influence on Lattice Constant

As a strong β -stabilizing (segregation) element, Fe atoms were supposed to redistribute between the secondary α precipitates and reverse-transformed β phase during the aging process at higher temperatures (\geq 500 °C). The redistributed Fe atoms would also be largely maintained in the α_s and retained β phase after water quench. To experimentally confirm this, STEM/EDX characterizations (Figure 5) were conducted on the initial microstructure as well as those aged at 600 °C, 650 °C, and 700 °C. In the STEM dark-field images [Figures 5(a) ~ (d)], both equiaxed α grains and α_s can be clearly distinguished from the retained β phase due to a dramatically different Fe concentrations. The corresponding Fe mappings are shown in Figures 5(e) ~ (h), and the average Fe concentrations of α_s and retained β phase in different microstructures are summarized in Table I. In the initial microstructure, the average Fe concentration of β phase is 4.6 wt pct. With the advent of secondary α precipitates that were depleted in Fe, most of the Fe atoms were rejected into the retained β phase, leading to a much higher Fe concentration (18.0 wt pct) of the retained β phase in specimen aged at 600 °C [Figure 5(f) and Table I]. With increasing aging temperature, although the average Fe concentration of retained β phase gradually decreased (from 18.0 wt pct to 7.4 pct) due to a continuously increased volume fraction of retained β phase, they were still much larger than the Fe concentration of β phase in the initial microstructure.

Due to a smaller atomic radius of substitutional Fe (0.126 nm) than Ti matrix (0.147 nm), a higher Fe concentration of retained β phase would result in a reduced lattice constant. Moreover, the athermal ω phase transformed from β phase by a diffusionless, displacive mechanism,^[24,30] in which the following relationship between the lattice constants of β phase and resulting athermal ω phase was followed:

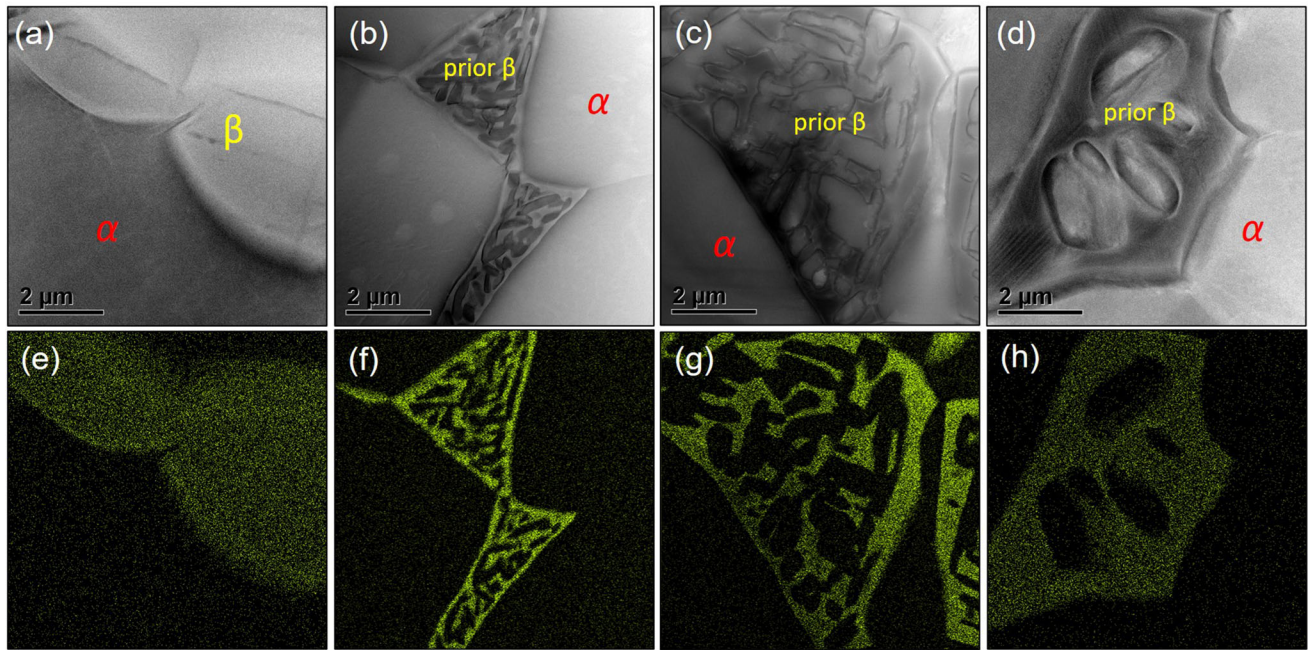


Fig. 5—STEM dark-field images (a) ~ (d) and corresponding Fe mappings (e) ~ (h) of Ti-1.0Fe alloy before aging (a), (e) as well as aged at 600 °C (b), (f); 650 °C (c), (g) and 700 °C (d), (h). Regions with higher Fe concentrations corresponded to the retained β . The Fe concentrations of retained β gradually decreased with increasing aging temperature, though they remained much larger than that in the initial microstructure.

Table I. Average Fe Concentrations of the α_s and Retained β Phase in the Initial Microstructure and Those Aged at 600 °C, 650 °C, and 700 °C

	Initial microstructure (percent)	600 °C (percent)	650 °C (percent)	700 °C (percent)
Wt pct (Fe) of retained β	4.6	18.0	13.1	7.4
Wt pct (Fe) of α_s precipitates	—	0.27	0.23	0.20

$$a_{\omega} = \sqrt{2}a_{\beta} \text{ and } c_{\omega} = \left(\frac{\sqrt{3}}{2}\right)a_{\beta}$$

Therefore, it is reasonable to assume that the lattice constant of resulting athermal ω phase also gradually decreased with increasing Fe concentration. This could explain the pronounced peak shift of ω phase from the aging temperature of 600 °C to 700 °C. For example, the much higher Fe concentration (18.0 wt pct) of retained β phase in the 600 °C aged microstructure led to a much smaller lattice constant of athermal ω phase than those in the initial microstructure. This led to a substantial peak shift ($\sim 0.5^\circ$ to the right-hand side direction) of athermal ω phase in the XRD pattern, as compared to its original position in the initial microstructure (Figure 3). At higher aging temperatures (650 °C and 700 °C), the Fe concentrations of retained β phase gradually decreased and consequently the lattice constants of resulting athermal ω phase also gradually increased. As a result, a gradual peak shift of ω phase towards a smaller 2θ angle was observed in the XRD patterns. Nevertheless, even at the highest aging temperature (700 °C), the peak position of ω phase was still at a 2θ angle larger than its original position due to a relatively higher level of Fe concentration in the retained

β phase. In addition, the volume fraction of athermal ω phase was believed to be proportional to the volume fraction of retained β phase from which it transformed. Thus, a slightly increased peak intensity of ω phase was also identified as the aging temperature increased from 600 °C to 700 °C (Figure 3).

C. Evolution of Nano-hardness with Aging Temperature

Together with the phase transformation and microstructural evolution occurred during aging, the local mechanical properties of equiaxed α grains and prior β areas (including α_s and retained β) also changed accordingly. The average nano-hardness values of the two areas are plotted against the aging temperature (Figure 6). Before aging, the β grains were about three times harder than α grains, which have been attributed to the precipitation hardening of extremely fine ω_{ath} and solid solution hardening of Fe atoms.^[5] Until the aging temperature of 400 °C, the nano-hardness of prior β areas remained nearly the same. This suggested that the transformation from athermal ω phase into thermal ω phase as well as related Fe diffusion from ω precipitates into β matrix had a negligible influence on the precipitation hardening effect of these nano-sized precipitates on prior β areas. At the aging temperature of 500 °C, where the nano-sized ω precipitates were replaced by

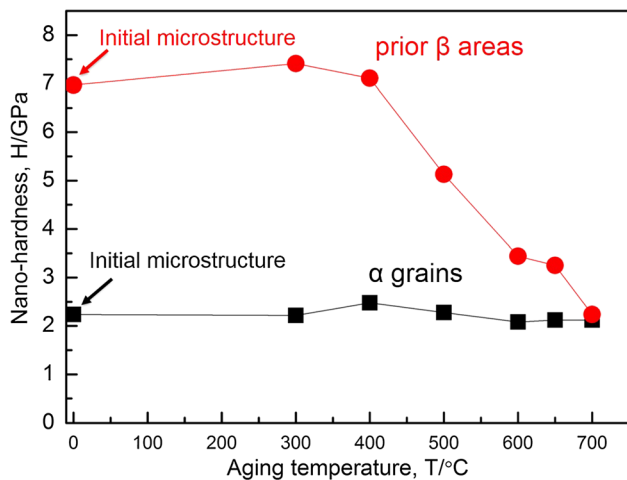


Fig. 6—The evolution of nano-hardness of α grains and prior β areas in Ti-1.0Fe alloy with aging temperature. Gradual softening of prior β areas was observed when the aging temperatures were higher than 400 °C.

plate-shaped secondary α precipitates, there was a sudden drop of the nano-hardness of prior β areas. This indicates that the hardening effect of secondary α precipitates was much weaker than those from nano-sized ω_{ath} . Two possible explanations can be suggested for this hardness evolution tendency. First, the size of ω_{ath} precipitates was generally around 20 nm, one order of magnitude finer than that of secondary α precipitates [typically 200 ~ 1000 nm wide, and several micrometers long, as shown in Figures 4(c)–(h)]. Therefore, there will be much more interphase boundaries in the initial microstructure ($\beta/\omega_{\text{ath}}$ interphase boundary) than in the aged microstructures (β/α_s interphase boundary), which will result in a much higher barricade in the former microstructure against dislocation movement during the indentation tests. Second, the Fe concentration of ω_{ath} precipitates (4.6 wt pct, same as the β phase) in the initial microstructure was much higher than that of α_s precipitates (≤ 0.27 wt pct, as measured by EDAX shown in Figure 5). Fe is the main solid solution hardening element in Ti-1.0 wt pct Fe alloy. Hence, the dramatic difference in solid solution element concentrations between ω_{ath} precipitates and α_s precipitates will also play a role in the different nano-hardness between the two microstructures.

With further increasing aging temperature, the nano-hardness of prior β areas decreased furthermore, which can be ascribed to the gradual coarsening of α_s . Nevertheless, the prior β areas remained slightly harder than α grains even at the highest aging temperature. In comparison, the nano-hardness of α grains remained nearly the same for all the aging temperatures, which indirectly confirmed the absence of phase transformation inside the α phase during aging.

D. Influence of Athermal ω on the Precipitation Behavior of Secondary α Phase

In the preceding section, the detailed microstructure evolution and phase transformation occurred during aging (300 °C ~ 700 °C) of Ti-1.0 wt pct Fe alloy with a dual-phase initial microstructure have been systematically investigated. It was found that secondary α precipitates began to appear inside the β grains from the aging temperature of 500 °C, replacing the ω_{ath} in the initial microstructure. With a further increase of the aging temperature, the size of these secondary α precipitates continuously increased, while their number density and area fraction gradually decreased, owing to a partial α to β reverse phase transformation at higher aging temperatures. Notably, these secondary α precipitates generally exhibited a plate-shaped morphology with a rather weak variant selection (Figures 2 and 4), which was in sharp contrast to the α lamellar/colony structure typically found in $\alpha + \beta$ titanium alloys with similar intercritical annealing temperatures.^[31–34] Moreover, unlike the gradual coarsening of secondary α precipitates with aging temperature found in Ti-1.0Fe alloy, the thickness of α lamellae in typical lamellar/colony structure tended to slightly shrink at higher intercritical annealing temperatures. These microstructural discrepancies suggested a different precipitation behavior/mechanism for the secondary α precipitates in Ti-1.0Fe alloy with a dual-phase initial microstructure, when compared with that of conventional $\alpha + \beta$ titanium alloys. In particular, the pre-existing athermal ω precipitates inside the β grains of Ti-1.0Fe alloy was supposed to play a critical role.

In order to clarify the influence of ω_{ath} on the subsequent precipitation behaviors of α_s in Ti-1.0 wt pct Fe alloy, two different thermomechanical-processing (TMP) routes were specifically designed, as illustrated in Figure 7. In route (a) [Figure 7(a)], the specimens after hot deformation were firstly water quenched to room temperature and then reheated to the aging temperature (650 °C), holding for 1 minute (specimen ①) or 60 minutes (specimen ②) followed by water quench. In this case, the microstructure before aging already contained athermal ω precipitates (similar to those in the results section). Specimens ① and ② represented the early and steady stages of secondary α precipitation process in route (a), respectively. In route (b) [Figure 7(b)], the specimens after hot deformation were *directly* quenched ($20 \text{ }^\circ\text{C s}^{-1}$) to the aging temperature (650 °C) and held for 1 minute (specimen ③) or 60 minutes (specimen ④) followed by water quench. The aging temperature was chosen to be well above the ω solvus temperature (400 °C to 500 °C) of Ti-1.0Fe alloy, so that the secondary α precipitation behavior was not affected by athermal ω precipitates in this route. Specimens ③ and ④ represented the early and steady stages of secondary α precipitation process in route (b), respectively. The phase maps (α phase: red, β phase: green) of obtained microstructures are shown in Figures 7(c) ~ (f). The corresponding inverse pole figure (IPF) maps of α phase in the rectangle areas are shown in Figures 7(g) ~ (j), respectively.

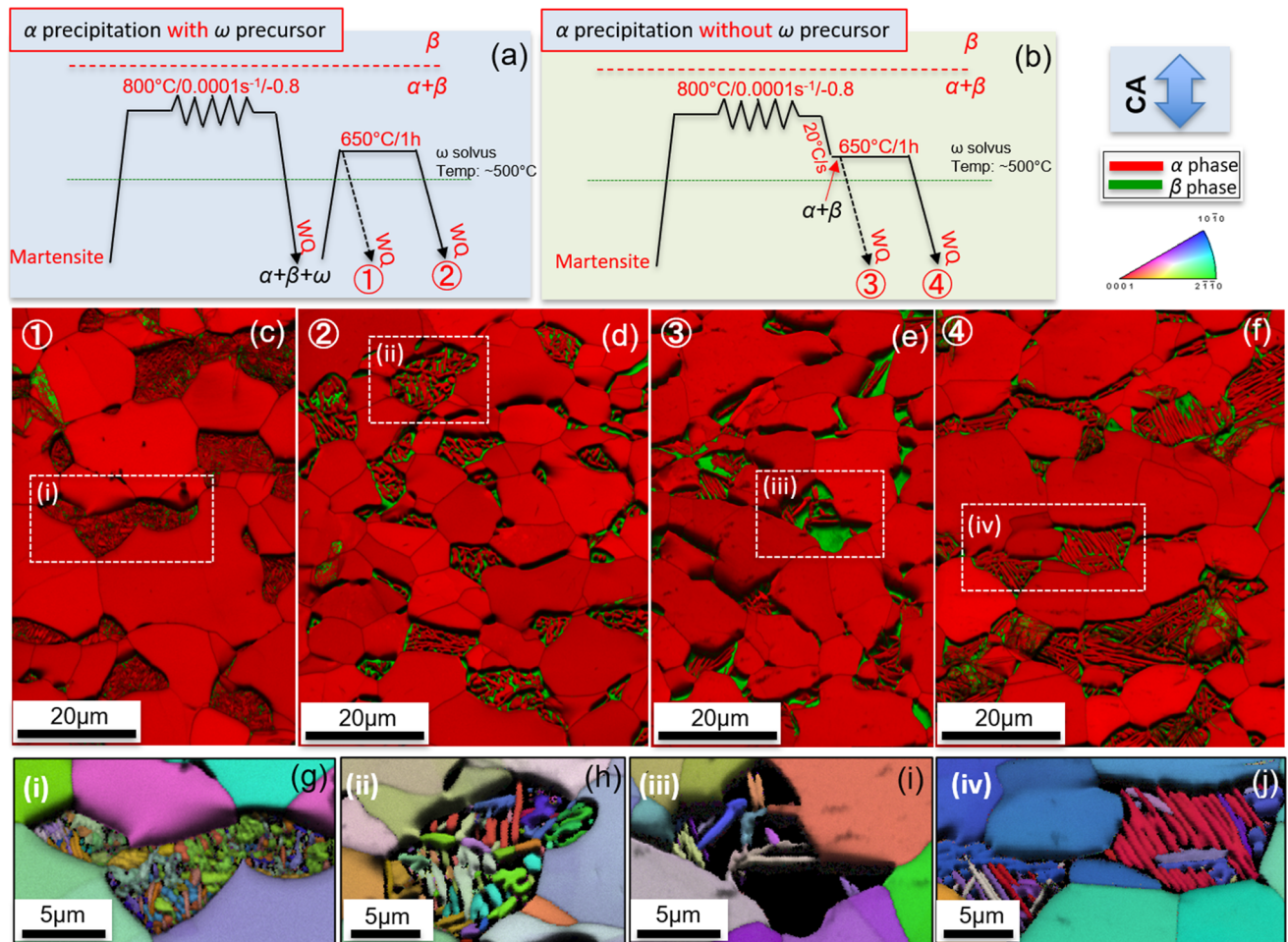


Fig. 7—Influence of athermal ω precipitates on the secondary α phase precipitation behaviors in Ti-1.0Fe alloy. In TMP route (a), the specimens after hot deformation were immediately water quenched to room temperature and then reheated to 650 °C and held for 1 minute (①) and 60 minutes (②) followed by water quenching. In TMP route (b), the specimens after hot deformation were directly quenched (20 °C·s⁻¹) to 650 °C and held for 1 minute (③) and 60 minutes (④) followed by water quenching. Phase maps (α phase: red, β phase: green) of the obtained microstructures are shown in (c) ~ (f). IPF maps of α phase showing the microstructural features in the rectangle areas in phase maps are given in (g) ~ (j). The compression direction was vertical for all the microstructures (Color figure online).

In route (a), where the microstructure before aging already contained athermal ω precipitates, the β grains were readily fully occupied with secondary α precipitates at the early stage of aging [Figure 7(c)]. These ultra-fine-grained secondary α precipitates with a nearly equiaxed morphology exhibited various crystallographic orientations [Figure 7(g)]. With increasing aging time [Figure 7(d)], the size of these secondary α precipitates substantially increased, whereas their aspect ratio (length/width) remained low and more importantly, the variety in crystallographic orientations was also maintained [Figure 7(h)]. As a matter of fact, no lamellar/colony structure has ever been found in route (a) even after longer aging times. In comparison, for route (b) where the microstructure did not contain athermal ω precipitates before aging, the precipitation behavior as well as its evolution tendency with aging time was dramatically different. Specifically, at the early stage of aging [Figures 7(e) and (i)], a few secondary α precipitates with a lamellar morphology were observed nucleating either from the equiaxed α grains or along the

β grain boundaries. Some of the α lamellae also grew from the grain boundary α into neighboring β grains. The volume fraction of secondary α lamellae at the early stage of aging [Figure 7(e) and (i)] was much lower than that with the same aging time in route (a) [Figure 7(c) and (g)]. With a longer aging time in route (b) [Figures 7(f) and (j)], the typical lamellar/colony structure was formed, and within a colony, aggregates of parallel α lamellae with the same crystallographic orientation were observed. The thickness of secondary α lamellae, however, remained nearly the same as those at the early stage of aging. The size of some colonies, for example, the one with red color in the IPF map [Figure 7(j)], was much larger than the others, suggesting a preferential growth of some colonies with specific crystallographic orientations. The volume fractions of secondary α lamellae/precipitates at the steady stages of aging were nearly the same for both TMP routes.

In titanium alloys, the Burgers orientation relationship (OR) ($\{0001\}_{\alpha} // \{110\}_{\beta}$, $\langle 11-20 \rangle_{\alpha} // \langle 111 \rangle_{\beta}$) is followed during the β to α phase transformation, and

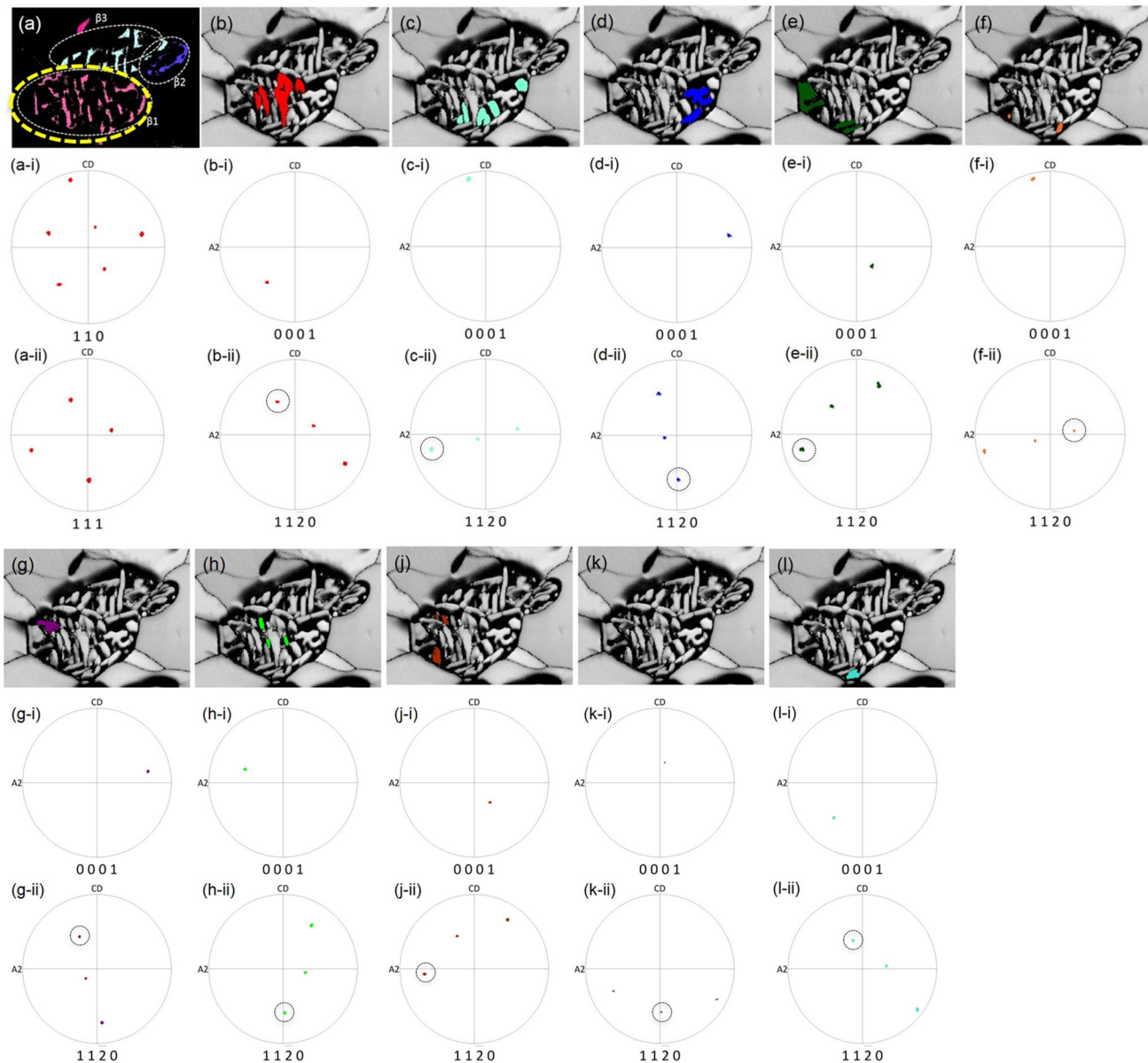


Fig. 8—Crystallographic OR analysis between the secondary α precipitates and parent β grain in sample ② following the thermomechanical-processing route (a). The (110) (a-i) and (111) (a-ii) pole figures of β grain (a) on the lower part of the figure as well as the (0002) [(b-i) ~ (f-i)] and (11-20) [(b-ii) ~ (f-ii)] pole figures of secondary α precipitates (b-f) inside the β grain are shown. Totally 10 variants of secondary α precipitates with almost equal population were identified inside this β grain.

there are totally 12 possible α variants transforming from a parent β grain.^[35] The crystallographic OR between secondary α lamellae/precipitates and parent β grains at the steady stages of aging (specimen ② and ④) were analyzed and compared. In specimen ②, secondary α precipitates inside the β grain on the lower part of Figure 8(a) (marked by yellow dashed lines) were investigated. The corresponding (110) and (111) pole figures of β phase as well as the (0002) and (11-20) pole figures of α phase are shown in Figure 8. It was confirmed that all these secondary α precipitates followed the Burgers OR with parent β grain, and totally 10 out of the 12 possible α variants were identified in this β grain. Moreover, these 10 variants had a nearly equal population, suggesting a rather weak variant selection

during the β to α phase transformation following route (a), in other words, on conditions *with* the influence of athermal ω precipitates. In specimen ④, secondary α lamellae inside the β grain on the right part of Figure 9(a) (marked by yellow dashed lines) were investigated. The corresponding (110) and (111) pole figures of β phase as well as the (0002) and (11-20) pole figures of α phase are shown in Figure 9. All these secondary α lamellae also maintained the Burgers OR with parent β grain, but only five variants were found for them. Furthermore, one of the variants [the α lamellae with a red color in Figure 9(b)] was dominant size for this variant. These microstructural characteristics suggested a strong variant selection during the β to α

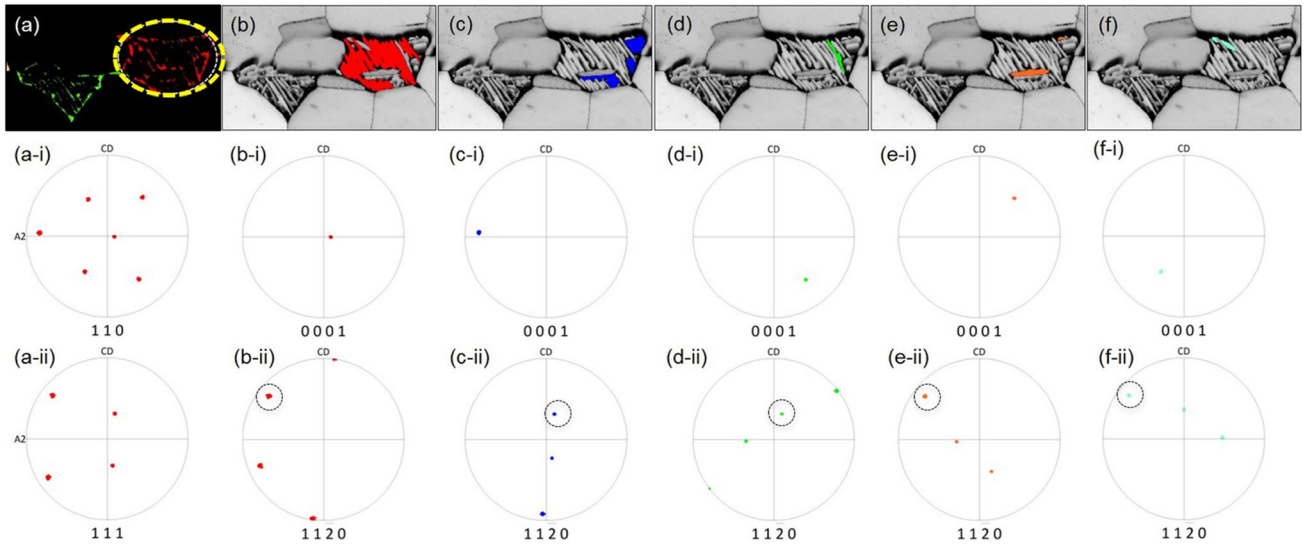


Fig. 9—Crystallographic OR analysis between the secondary α lamellae and parent β grain in sample ④ following the thermomechanical-processing route (b). The (110) (a-i) and (111) (a-ii) pole figures of β grain (a) on the right part of the figure as well as the (0002) [(b-i) ~ (f-i)] and (11-20) [(b-ii) ~ (f-ii)] pole figures of secondary α lamellae (b-f) inside the β grain are shown. Only five variants of secondary α lamellae were identified inside this β grain and one of them exhibited substantial preferential growth (Color figure online).

phase transformation following route (b), in other words, on conditions *without* the influence of athermal ω precipitates.

Based on the microstructural characterization and crystallographic orientation analysis described above, it can be concluded that the existence of ω_{ath} in the initial microstructure of Ti-1.0Fe alloy indeed strongly affects the size, morphology, and crystallographic orientations of secondary α precipitates formed during subsequent aging process. Specifically speaking, when the initial microstructure contains ω_{ath} before aging [*e.g.*, in route (a)], these fine ω_{ath} will act as the nucleation sites for the secondary α precipitates, following the athermal ω —thermal ω —secondary α phase transformation sequence. The uniformly distributed nano-sized ω_{ath} promotes a homogeneous precipitation behavior of α_s inside β grains. Thus, ultrafine-grained secondary α precipitates with a large number density form readily at the early stage of aging. Since not directly transforming from the parent β phase, a rather weak variant selection can be found for these secondary α precipitates, which has been manifested by a nearly random crystallographic orientation distribution as well as a low aspect ratio of these precipitates. With increasing aging time, a gradual coarsening of these secondary α precipitates as well as a partial α to β reverse phase transformation occurs. Nevertheless, the random crystallographic orientation distribution and low aspect ratios of the secondary α precipitates can still be maintained even after prolonged aging times. It should also be pointed out that despite of the complicated β phase—athermal ω —thermal ω —secondary α phase transformation sequence, the Burgers OR between secondary α precipitates and parent β grain is still strictly followed (Figure 8). In comparison, when the initial microstructure does not contain athermal ω precipitates before aging, [*e.g.*, in route (b)], the classical heterogeneous

precipitation mechanism of secondary α phase is obeyed.^[36–45] In this context, secondary α phase firstly nucleates either along the β grain boundaries or epitaxially from the equiaxed α grains. The epitaxially grown secondary α phase typically exhibited the same crystallographic orientation with parent equiaxed α grains. The grain boundary α phase follows the Burgers OR with one of the neighboring β grains but not both of them.^[37–39] The grain boundary α phase then grows into the neighboring β grain with Burgers OR in the form of α lamellae in order to minimize the interface energy [Figure 7(i)]. During this process, a strong variant selection of secondary α lamellae takes places, and there exists a specific orientation relationship between the secondary α lamellae and the grain boundary α phase from which they grow.^[37–39] Also, in this case, the secondary α precipitation kinetics at the early stage of aging was much slower compared with that in the homogeneous precipitation case in route (a). With prolonged aging time, the repetition of nucleation and growth of secondary α lamella from grain boundary α phase results in the formation of α lamellar/colony structure with only limited crystallographic orientations [Figure 7(j)]. There is also a preferential growth of some colonies with specific orientations, leading to a much larger colony size for that orientation.

IV. CONCLUSIONS

In this study, the aging behavior (300 °C ~ 700 °C) of Ti-1.0Fe alloy with an equiaxed $\alpha + \beta$ initial microstructure was systematically investigated by employing comprehensive microstructural characterization and micromechanical property testing techniques. In particular, the influence of athermal ω precipitates in the initial microstructure on the precipitation behavior

of secondary α phase was evaluated through specifically designed TMP routes. Based on the experimental results and discussion, the following conclusions can be drawn.

- (1) The solvus temperature of athermal ω precipitates in Ti-1.0Fe alloy was determined to be ~ 500 °C, above which secondary α precipitates appeared inside the β grain. These ultrafine secondary α precipitates underwent coarsening and a partial α to β reverse phase transformation with increasing aging temperature. The gradual dissolution of ω_{ath} together with the subsequent coarsening of α_s resulted in a continuous softening of prior β areas with increasing aging temperature.
- (2) There was a redistribution of Fe atoms between α_s and retained β phase at temperatures higher than 600 °C, in which the Fe concentration of retained β phase was much higher. Consequently, the athermal ω precipitates inheriting the high Fe concentration of retained β phase showed a much smaller lattice constant than that in the initial microstructure.
- (3) The athermal ω precipitates promoted a homogeneous precipitation behavior by providing more intragranular nucleation sites for secondary α precipitates. This led to a formation of secondary α precipitates with a smaller aspect ratio and a much weaker variant selection. In comparison, when secondary α phase directly transformed from β grain, the typical α lamellar/colony microstructure was obtained and a strong variant selection was observed.
- (4) The nano-hardness of prior β areas gradually decreased with increasing aging temperature, especially after the aging temperature of 400 °C. This can be attributed to a replacement of nano-sized athermal ω precipitates by secondary α precipitates, as well as their partial resolution at relatively higher aging temperatures. In comparison, the nano-hardness of α grains was stable throughout the aging process.

ACKNOWLEDGMENTS

The authors are grateful to the financial support from Cross-ministerial Strategic Innovation Promotion Program (SIP) supported by the Cabinet Office of Japanese government and the Elements Strategy Initiative for Structural Materials (ESISM) in Kyoto University supported by the Ministry of Education, Culture, Sports, Science and Technology (MEXT), Japan.

CONFLICT OF INTEREST

The authors declare that they have no known competing financial interests or personal relationships that could have appeared to influence the work reported in this study.

REFERENCES

1. D. Banerjee and J.C. Williams: *Acta Mater.*, 2013, vol. 61, pp. 844–79.
2. G. Lutjering and J.C. Williams: *Titanium*, 2nd ed. Springer, Berlin, 2007.
3. M. Peters and C. Leyens: *Titanium and titanium alloys-fundamentals and applications*, Wiley, Hoboken, 2003.
4. G. Lutjering: Influence of processing on microstructure and mechanical properties of ($\alpha + \beta$) titanium alloys. *Mater. Sci. Eng. A*, 1998, vol. 243, pp. 32–45.
5. Y. Chong, R.X. Zheng, G.Y. Deng, A. Shibata, and N. Tsuji: *Metall. Mater. Trans. A*, 2020, vol. 51, pp. 2851–862.
6. J. Umeda, T. Tanaka, T. Teramae, S. Kariya, J. Fujita, H. Nishikawa, Y. Shibutani, J.H. Shen, and K. Kondoh: *Mater. Sci. Eng. A*, 2021, vol. 803, p. 140708.
7. G.Y. Deng, T. Bhattacharjee, Y. Chong, R.X. Zheng, Y. Bai, A. Shibata, and N. Tsuji: *J. Alloys Compd.*, 2020, vol. 822, p. 153604.
8. A.R. Kilmametov, Yu. Ivanisenko, A.A. Mazilkin, B.B. Straumal, A.S. Gornakova, O.B. Fabrichnaya, M.J. Kriegel, D. Rafaja, and H. Hahn: *Acta Mater.*, 2018, vol. 144, pp. 337–51.
9. B.B. Straumal, A.R. Kilmametov, Yu. Ivanisenko, A.S. Gornakova, A.A. Mazilkin, M.J. Kriegel, O.B. Fabrichnaya, B. Baretzky, and H. Hahn: *Adv. Eng. Mater.*, 2015, vol. 17, pp. 1835–841.
10. A. Kilmametov, Y. Ivanisenko, B. Straumal, A.A. Mazilkin, A.S. Gornakova, M.J. Kriegel, O.B. Fabrichnaya, D. Rafaja, and H. Hahn: *Scripta Mater.*, 2017, vol. 136, pp. 46–9.
11. Yu. Ivanisenko, A. Kilmametov, H. Rosner, and R.Z. Valiev: *Int. J. Mater. Res.*, 2018, vol. 99, pp. 36–41.
12. G.Y. Deng, T. Bhattacharjee, Y. Chong, R.X. Zheng, Y. Bai, A. Shibata, and N. Tsuji: *IOP Conf. Ser. Mater. Sci. Eng.*, 2017, vol. 194, p. 012020.
13. Y. Chong, G.Y. Deng, A. Shibata, and N. Tsuji: *Adv. Eng. Mater.*, 2019, vol. 21, p. 1900607.
14. M.J. Kriegel, A. Kilmametov, M. Rudolph, B.B. Straumal, A.S. Gornakova, H. Stocker, Y. Ivanisenko, O. Fabrichnaya, H. Hahn, and D. Rafaja: *Adv. Eng. Mater.*, 2018, vol. 20, p. 1700933.
15. H. Nakajima, K. Yusa, and Y. Kondo: *Scripta Mater.*, 1996, vol. 34, pp. 249–53.
16. H. Nakajima, S. Ohshida, K. Nonaka, Y. Yoshida, and F.E. Fujita: *Scripta Mater.*, 1996, vol. 34, pp. 949–53.
17. K. Majima, T. Hirata, M. Yamamoto, H. Nagai, and K. Shouji: *J. Jpn. Inst. Met.*, 1988, vol. 52, pp. 1113–120.
18. Y. Alshammari, S. Raynova, F. Yang, and L. Bolzoni: *Int. J. Refract. Met. H.*, 2020, vol. 90, p. 105246.
19. M.S. Oh, J.-Y. Lee, and J.K. Park: *Metall. Mater. Trans. A*, 2004, vol. 35, pp. 3071–077.
20. B.-Y. Chen, K.-S. Hwang, and K.-L. Ng: *Mater. Sci. Eng. A*, 2011, vol. 528, pp. 4556–563.
21. M. Yan, S.D. Luo, G.B. Schaffer, and M. Qian: *Metall. Mater. Trans. A*, 2013, vol. 44, pp. 3961–969.
22. S. Sandlobes, S. Korte-Kerzel, and D. Raabe: *Mater. Sci. Eng. A*, 2019, vol. 748, pp. 301–12.
23. Y. Chong, G.Y. Deng, Y. Zhang, N. Tsuji: *Unpublished*.
24. E. Sakedai, M. Shimoda, H. Nishizawa, and Y. Nako: *Mater. Trans.*, 2011, vol. 52, pp. 324–30.
25. Y.F. Zheng, R.E.A. Williams, D. Wang, R.P. Shi, S. Nag, P. Kami, J.M. Sosa, R. Banerjee, Y.Z. Wang, and H. Fraser: *Acta Mater.*, 2016, vol. 103, pp. 850–58.
26. Y.F. Zheng, R.E.A. Williams, J.M. Sosa, T. Alam, Y.Z. Wang, R. Banerjee, and H.L. Fraser: *Acta Mater.*, 2016, vol. 103, pp. 165–73.
27. Y.F. Zheng, R.E.A. Williams, J.M. Sosa, Y.Z. Wang, R. Banerjee, and H.L. Fraser: *Scripta Mater.*, 2016, vol. 111, pp. 81–4.
28. S. Nag, A. Devaraj, R. Srinivasan, R.E.A. Williams, N. Gupta, G.B. Viswanathan, J.S. Tiley, S. Banerjee, S.G. Srinivasan, H.L. Fraser, and R. Banerjee: *Phys. Rev. Lett.*, 2011, vol. 16, p. 245701.
29. B.S. Hickman: *J. Mater. Sci.*, 1969, vol. 4, pp. 554–63.
30. S.K. Sikka, Y.K. Vohra, and R. Chidambaram: *Prog. Mater. Sci.*, 1982, vol. 27, pp. 245–310.
31. Y. Chong, T. Bhattacharjee, and N. Tsuji: *Mater. Sci. Eng. A*, 2019, vol. 762, p. 138077.
32. Y. Chong, T. Bhattacharjee, R. Gholizadeh, J.H. Yi, and N. Tsuji: *Materialia*, 2019, vol. 8, p. 100480.
33. S.L. Semiatin, V. Seetharaman, and I. Weiss: *Mater. Sci. Eng. A*, 1999, vol. 263, pp. 257–71.

34. N. Stefansson, S.L. Semiatin, and D. Eylon: *Metall. Mater. Trans. A*, 2002, vol. 33, pp. 3527–534.
35. W.G. Burgers: *Physica*, 1934, vol. 1, pp. 561–86.
36. N. Stanford and P.S. Bate: *Acta Mater.*, 2004, vol. 52, pp. 5215–224.
37. D. Bhattacharyya, G.B. Viswanathan, and H.L. Fraser: *Acta Mater.*, 2007, vol. 55, pp. 8765–6778.
38. E. Lee, R. Banerjee, S. Kar, D. Bhattacharjee, and H.L. Fraser: *Philos. Mag.*, 2007, vol. 87, pp. 3615–627.
39. D. Bhattacharyya, G.B. Viswanathan, R. Denkenberger, D. Furrer, and H.L. Fraser: *Acta Mater.*, 2003, vol. 51, pp. 4679–691.
40. R. Shi, V. Dixit, H.L. Fraser, and Y. Wang: *Acta Mater.*, 2014, vol. 75, pp. 156–66.
41. R. Shi, V. Dixit, G.B. Viswanathan, H.L. Fraser, and Y. Wang: *Acta Mater.*, 2016, vol. 102, pp. 197–211.
42. T. Furuhashi, S. Takagi, H. Watanabe, and T. Maki: *Metall. Mater. Trans. A*, 1996, vol. 27, pp. 1635–646.
43. T. Furuhashi and T. Maki: *Mater. Sci. Eng. A*, 2001, vol. 312, pp. 145–54.
44. S.M.C. van Bohemen, A. Kamp, R.H. Petrov, L.A.I. Kestens, and J. Sijtsma: *Acta Mater.*, 2008, vol. 56, pp. 5907–914.
45. H. Beladi, Q. Chao, and G.S. Rohrer: *Acta Mater.*, 2014, vol. 80, pp. 478–89.

Publisher's Note Springer Nature remains neutral with regard to jurisdictional claims in published maps and institutional affiliations.

Springer Nature or its licensor (e.g. a society or other partner) holds exclusive rights to this article under a publishing agreement with the author(s) or other rightsholder(s); author self-archiving of the accepted manuscript version of this article is solely governed by the terms of such publishing agreement and applicable law.